ELSEVIER

Fluid Phase Equilibria 194–197 (2002) 197–206

FLUID PHASE EQUILIBRIA

www.elsevier.com/locate/fluid

Equilibria between solid, liquid, and vapor phases in binary Lennard–Jones mixtures

Monica H. Lamm, Carol K. Hall*

Department of Chemical Engineering, North Carolina State University, Box 7905, 113 Riddick Labs, Raleigh, NC 27695-7905, USA

Received 12 March 2001; accepted 14 September 2001

Abstract

We have used Monte Carlo simulation and the Gibbs–Duhem integration technique to calculate temperature–composition and pressure–temperature phase diagrams for binary Lennard–Jones mixtures. We systematically explore Lennard–Jones parameter space to demonstrate how the features of these phase diagrams change as a function of diameter ratio, well-depth ratio, binary interaction parameter, and pressure. We find a number of cases in which the vapor–liquid and liquid–liquid equilibria become metastable with respect to the solid–liquid and solid–vapor equilibria. © 2002 Elsevier Science B.V. All rights reserved.

Keywords: Molecular simulation; Phase equilibria; Solid–fluid equilibria; Lennard–Jones potential

1. Introduction

The phase equilibria displayed by binary mixtures has intrigued scientists and engineers for decades. Many investigators have predicted phase equilibria using a simple equation of state [1–6] or a combination of an intermolecular potential model and simulation [7–11] in order to develop intuition about the overall topography of phase diagrams for broad classes of substances. While most investigations of this nature have focused exclusively on fluid phase equilibria, in real systems, the appearance of the solid phase often has a big impact on the type of fluid phase equilibria observed because the solid phase interrupts the fluid phase [12].

To obtain a better overall picture of mixture phase behavior, one must consider all types of equilibrium between the vapor, liquid, and solid phases. In 1903, Smits [13] recognized that there are two categories of solid–fluid behavior which are distinguished by whether or not the solid–liquid–vapor coexistence curve interferes with the liquid–vapor critical curve. Within these two categories, Valyashko [14] identified 12 types of complete phase diagrams (i.e. showing equilibrium between solid, liquid, and vapor phases) for

* Corresponding author. Tel.: +1-919-5153571; fax: +1-919-5153465.
E-mail address: hall@turbo.che.ncsu.edu (C.K. Hall).

0378-3812/02/$ – see front matter
PII: S0378-3812(01)00650-1

binary mixtures. Most of Valyashko's types are based on experimental data for aqueous salt systems, but some were deduced by making educated guesses about the transitions in the topography between the experimentally known types. Luks and coworkers [15,16] have calculated complete phase diagrams for binary mixtures of solvent and a homologous series of solutes using the van der Waals equation of state and a simple solid state fugacity model. Vlot et al. [17] used a combination of molecular simulation and semi-empirical methods to calculate complete phase diagrams for symmetric (equal diameters, $\sigma_{11} = \sigma_{22}$; equal attractive well-depths, $\varepsilon_{11} = \varepsilon_{22}$) binary Lennard–Jones mixtures.

In this paper, we briefly review the results [18–20] of an investigation aimed at learning how intermolecular forces affect the equilibria between solid, liquid, and vapor phases in binary mixtures. We have calculated complete phase diagrams (i.e. showing equilibrium between solid, liquid, and vapor phases) for binary Lennard–Jones mixtures using Monte Carlo simulation and the Gibbs–Duhem integration method. This approach allows us to examine solid–liquid and solid–vapor phase behavior without resorting to a separate model for the solid state. In the first study [18], we calculated temperature–composition phase diagrams for 11 Lennard–Jones binary mixtures with diameter ratios $\sigma_{11}/\sigma_{22} = 0.85$–$1.0$ and attractive well-depth ratios $\varepsilon_{11}/\varepsilon_{22} = 0.625$–$1.6$, at a reduced pressure $P^* \equiv P\sigma_{11}^3/\varepsilon_{11} = 0.002$. Our focus in this study was on understanding how the interference between vapor–liquid and solid–liquid equilibria changes as a function of the molecular parameters. We also compared the resulting phase diagrams to those of real mixtures. In the second study [19], we calculated temperature–composition phase diagrams for three Lennard–Jones binary mixtures with diameter ratio $\sigma_{11}/\sigma_{22} = 0.85$, well-depth ratio $\varepsilon_{11}/\varepsilon_{22} = 0.45$, and binary interaction parameters $\delta_{12} = 1.0$, 0.9, and 0.75, at reduced pressure, $P^* = 0.05$. Our focus in this study as on determining if and when regions of liquid–liquid coexistence are metastable with respect to regions of solid–fluid coexistence. In the third study [20], we calculated temperature–composition phase diagrams for six binary Lennard–Jones mixtures with diameter ratios $\sigma_{11}/\sigma_{22} = 0.85$, 0.9, and 0.95 and well-depth ratios $\varepsilon_{11}/\varepsilon_{22} = 0.45$ and 1.6 at reduced pressures $P^* = 0.002$–0.1. Our focus in this study was on learning how the pressure–temperature projections of the resulting phase diagrams, particularly, the three-phase coexistence curves, shift with diameter ratio and well-depth ratio.

The remainder of this article is organized in the following manner. In Section 2, we give a short description of the Gibbs–Duhem integration method used to calculate the complete phase diagrams. In Section 3, we review selected results from the three studies mentioned above. We conclude in Section 4 with a brief summary.

2. Method

The coexistence lines in all three studies were calculated using Gibbs–Duhem integration [21,22]. In this method, phase coexistence is determined by integrating the Clapeyron differential equation. The Clapeyron equation for equilibrium between two binary phases (α and γ) at constant pressure is

$$\frac{\mathrm{d}\beta}{\mathrm{d}\xi_2} = \frac{(x_2^\alpha - x_2^\gamma)}{\xi_2(1-\xi_2)(h^\alpha - h^\gamma)}, \tag{1}$$

where β is the reciprocal temperature, $1/kT$, with k the Boltzmann constant and T the absolute temperature, ξ_2 the fugacity fraction of species 2, $\xi_2 = f_2/\sum f_i$, with f_i the fugacity of species i in solution, x_2 the mole fraction of species 2, and h is the molar enthalpy. The right-hand side of Eq. (1) can be integrated numerically to find an equation for β as a function of ξ_2 if we have an initial condition describing the temperature, fugacity fraction, enthalpies, and compositions at one coexistence point.

In our work, a convenient choice for the initial coexistence condition is the vapor–liquid or solid–liquid equilibrium condition for either of the pure components. The vapor–liquid and solid–liquid coexistence data for a single component Lennard–Jones system have been obtained via Gibbs–Duhem integration [22,23]. The slope of the integrand in Eq. (1) is undefined for pure components ($\xi_2 = 0$, $x_2 = 0$ or $\xi_2 = 1$, $x_2 = 1$), but it can be estimated using the limiting case of infinite dilution. This procedure is described elsewhere [18,24,25] and will not be reviewed here.

The enthalpies and mole fractions needed for the integration of Eq. (1) were obtained by semi-grand canonical Monte Carlo simulation [26] (constant temperature, pressure, total number of molecules, and fugacity fraction) on the two phases. The simulations were run with a system size of 500 particles per phase. An fcc crystalline structure was maintained in the solid phase by imposing a single occupancy constraint [27,28] on the trial displacement of particles in the solid. The pressure was held constant and the temperature and fugacity fraction were varied according to the values specified by the predictor–corrector algorithm used to numerically integrate Eq. (1).

In some of the mixtures, we encountered occurrences of three-phase lines, such as is found for a heteroazeotrope (liquid–liquid–vapor). In this case, two Gibbs–Duhem integrations were conducted, each starting from the vapor–liquid coexistence condition of the pure components ($x_2 = 0$ and $x_2 = 1$). At some x_2 (unknown at the commencement of the two integrations), the vapor phase coexistence lines will cross, thus determining the temperature, fugacity fraction, and coexistence compositions of the three coexisting phases: liquid(1), liquid(2), and vapor. The liquid phase mole fractions and enthalpies then become the initial condition for the liquid–liquid coexistence curve found below the heteroazeotrope temperature.

3. Results

We began by exploring the effect that changes in both molecular size and intermolecular attractions have on the complete temperature–composition phase behavior of a Lennard–Jones mixture at a single pressure [18]. We calculated complete phase diagrams for binary Lennard–Jones mixtures with diameter ratios $\sigma_{11}/\sigma_{22} = 0.85$–$1.0$ and attractive well-depth ratios $\varepsilon_{11}/\varepsilon_{22} = 0.625$–$1.6$, at a reduced pressure $P^* \equiv P\sigma_{11}^3/\varepsilon_{11} = 0.002$ which is equivalent to atmospheric pressure for argon. The cross-species interaction parameters were obtained from Lorentz–Berthelot combining rules, $\sigma_{12} = (\sigma_{11} + \sigma_{22})/2$ and $\varepsilon_{12} = (\varepsilon_{11}\varepsilon_{22})^{1/2}$. We restricted ourselves to diameter ratios ranging from 0.85 to 1.0 because calculations on binary hard sphere mixtures [29–32] have shown that the stable phase in this region is a substitutionally disordered fcc solid solution (the two species pack onto the same fcc crystalline lattice and can substitute for one another in any order on the lattice). At diameter ratios less than 0.85, the calculation is more complex because several ordered crystalline phases are possible, necessitating the calculation of each phase's free energy to determine the most stable crystalline structure.

Fig. 1 shows the temperature–composition phase diagram calculated for the binary Lennard–Jones mixture with $\sigma_{11}/\sigma_{22} = 0.90$ and $\varepsilon_{11}/\varepsilon_{22} = 0.625$, along with a not-to-scale schematic to illustrate the features of the phase diagram more clearly. Vapor–liquid coexistence lines originate from pure component 2 ($x_2 = 1$, $T^* = 1.157$) and decrease in temperature with decreasing fugacity fraction ξ_2. Liquid–solid coexistence lines originate from pure component 2 ($x_2 = 1$, $T^* = 1.099$) and decrease in temperature with decreasing fugacity fraction ξ_2. The vapor–liquid and liquid–solid curves meet at $T^* = 1.086$ and form a three-phase, vapor–liquid–solid equilibrium line. Vapor–solid coexistence lines originate from this

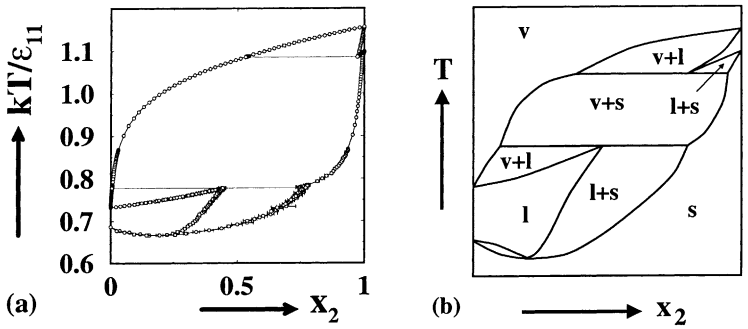

Fig. 1. Temperature–composition phase diagram for a binary Lennard–Jones mixture with diameter ratio of 0.90 and a well-depth ratio of 0.625 at a reduced pressure of $P^* = 0.002$ [18]. (a) Phase diagram obtained via Gibbs–Duhem integration. The circles represent data from the Gibbs–Duhem integration simulations. Error bars are shown when they are larger then the width of the symbol. Lines are drawn through the points for clarity. (b) Schematic phase diagram corresponding to (a). The labels identifying the phases present in each region are as follows: v (vapor), l (liquid), and s (fcc solid solution).

three-phase line and decrease in temperature with decreasing fugacity fraction. Vapor–liquid curves originate from pure component 1 ($x_2 = 0$, $T^* = 0.732$) and increase in temperature with increasing fugacity fraction. The vapor–liquid and vapor–solid curves meet at $T^* = 0.770$ and form another three-phase, vapor–liquid–solid equilibrium line. Liquid–solid coexistence lines originate from this three-phase line and decrease in temperature with decreasing fugacity fraction ξ_2 to a minimum melting point ($x_2 = 0.195$, $T^* = 0.665$). The solid–liquid lines then increase in temperature with decreasing fugacity fraction ξ_2 until they reach the solid–liquid coexistence temperature for pure component 1 ($x_2 = 0$, $T^* = 0.687$). A miscible solid phase exists below the solid–liquid curves.

Schematic phase diagrams based on the simulation results for this study [18] are shown in Fig. 2. We find that for well-depth ratios of unity (equal attractions among species), there is no interference between the vapor–liquid and solid–liquid coexistence regions. As the well-depth ratio increases or decreases from unity, the vapor–liquid and solid–liquid phase envelopes widen and interfere with each other leading to a solid–vapor coexistence region. For all well-depth ratios and a diameter ratio of 0.95, the solid–liquid lines have a shape characteristic of a solid solution (with or without a minimum melting temperature); as the diameter ratio decreases the solid–liquid lines fall to lower temperatures until they eventually drop below the solid–solid coexistence region, resulting in either a eutectic or peritectic three-phase line.

There are many examples of real mixtures that display phase diagrams that are qualitatively similar to the phase diagrams for the Lennard–Jones binary mixtures shown in Fig. 2. The binary mixture *p*-dichlorobenzene–*p*-dibromobenzene [33–35] has a temperature–composition phase diagram like the one calculated for $\sigma_{11}/\sigma_{22} = 0.95$ and $\varepsilon_{11}/\varepsilon_{22} = 0.625$. The similarities between this real mixture and the Lennard–Jones mixture can be explained by noting that both *p*-dichlorobenzene and *p*-dibromobenzene are symmetric molecules and that they differ in size by approximately 6% along their longest linear dimension [36]. Other examples include: argon–krypton [37–39] resembling the $\sigma_{11}/\sigma_{22} = 0.90$, $\varepsilon_{11}/\varepsilon_{22} = 1.0$ mixture; water–sodium chloride, water–silver nitrate [40,41], and methane–*n*-hexadecane [42] resembling the $\sigma_{11}/\sigma_{22} = 0.85$, $\varepsilon_{11}/\varepsilon_{22} = 0.625$ mixture; and iodine–sulfur [43] resembling the $\sigma_{11}/\sigma_{22} = 0.85$, $\varepsilon_{11}/\varepsilon_{22} = 0.625$ mixture.

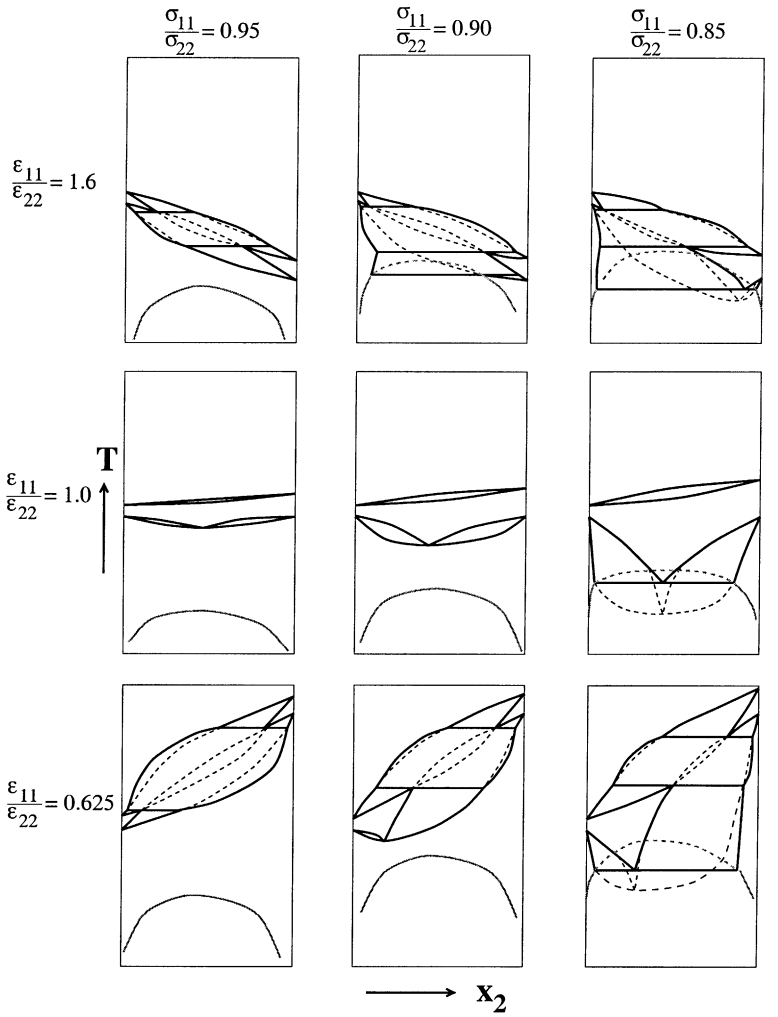

Fig. 2. Schematic phase diagrams based on the simulation results obtained in [18]. The columns correspond to mixtures with diameter ratios of 0.95, 0.9, and 0.85, and the rows correspond to mixtures with well-depth ratios of 1.6, 1.0, and 0.625. Heavy lines correspond to the equilibrium curves calculated by the Gibbs–Duhem integration simulations [18]. Thinner lines represent solid–solid coexistence curves that have been estimated using quasi-chemical theory arguments. Metastable coexistence curves are indicated with dashed lines.

Next we explored the effect that changes in the binary interaction parameter $\delta_{12} \equiv \varepsilon_{12}/(\varepsilon_{11}\varepsilon_{22})^{1/2}$, i.e. deviations in the Lorentz–Berthelot combining rule, have on the complete phase behavior of a mixture at constant pressure [19]. Complete diagrams were calculated for binary Lennard–Jones mixtures with diameter ratio $\sigma_{11}/\sigma_{22} = 0.85$, well-depth ratio $\varepsilon_{11}/\varepsilon_{22} = 0.45$, and binary interaction parameters $\delta_{12} = 1.0, 0.9,$ and 0.75, at reduced pressure, $P^* = 0.05$. For the mixture with $\delta_{12} = 1.0$, we find a spindle-shaped vapor–liquid coexistence region and a eutectic solid–liquid coexistence region separated by a completely miscible liquid phase, similar to Fig. 2 (center, right). For the mixtures with $\delta_{12} < 1$, we find that the vapor–liquid and solid–liquid coexistence regions interfere resulting in a vapor–solid coexistence region

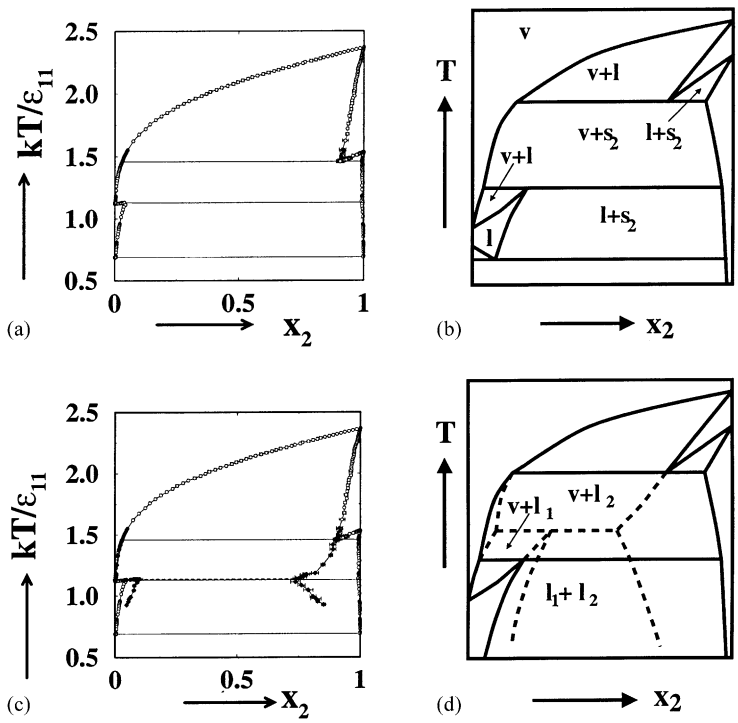

Fig. 3. Temperature–composition phase diagram for a binary Lennard–Jones mixture with diameter ratio of 0.85 and a well-depth ratio of 0.45 at a reduced pressure of $P^* = 0.05$ [19]. (a) Phase diagram obtained via Gibbs–Duhem integration. The open circles represent data from the Gibbs–Duhem integration simulations. Error bars are shown when they are larger then the width of the symbol. Lines are drawn through the points for clarity. (b) Schematic phase diagram corresponding to (a). The labels identifying the phases present in each region are as follows: v (vapor), l (liquid), s_1 (fcc solid solution rich in component 1), and s_2 (fcc solid solution rich in component 2). (c) Phase diagram showing the metastable vapor–liquid and liquid–liquid equilibria along with the equilibrium coexistence curves of (a). The open circles (equilibrium) and filled diamonds (metastable) represent data from the Gibbs–Duhem integration simulations. The dashed line indicates the metastable heteroazeotrope. (d) Schematic phase diagram corresponding to (c). The solid lines indicate the equilibrium coexistence curves and the dashed lines indicate the metastable coexistence curves. The labels identifying the metastable phases are as follows: v (vapor), l_1 (liquid rich in component 1), and l_2 (liquid rich in component 2).

bounded above and below by solid–liquid–vapor coexistence lines. We also find that the mixtures with $\delta_{12} < 1$ have a region of liquid–liquid immiscibility that is metastable with respect to the solid–fluid phase equilibria. These feature are illustrated in Fig. 3 which shows the temperature–composition phase diagram calculated for the binary Lennard–Jones mixture with $\sigma_{11}/\sigma_{22} = 0.85$, $\varepsilon_{11}/\varepsilon_{22} = 0.45$, and $\delta_{12} = 0.9$. Both the equilibrium and the metastable coexistence curves are shown, along with not-to-scale schematics.

We have also explored the effect that varying the pressure has on the complete phase behavior of a mixture [20]. Temperature–composition phase diagrams have been calculated for six binary Lennard–Jones mixtures with diameter ratios $\sigma_{11}/\sigma_{22} = 0.85$, 0.9, and 0.95 and well-depth ratios $\varepsilon_{11}/\varepsilon_{22} = 0.45$ and 1.6 at reduced pressures $P^* = 0.002$–0.1. In Fig. 4, the temperature–composition phase diagrams for the binary Lennard–Jones mixture with ratios $\sigma_{11}/\sigma_{22} = 0.85$ and $\varepsilon_{11}/\varepsilon_{22} = 1.6$ at reduced pressures

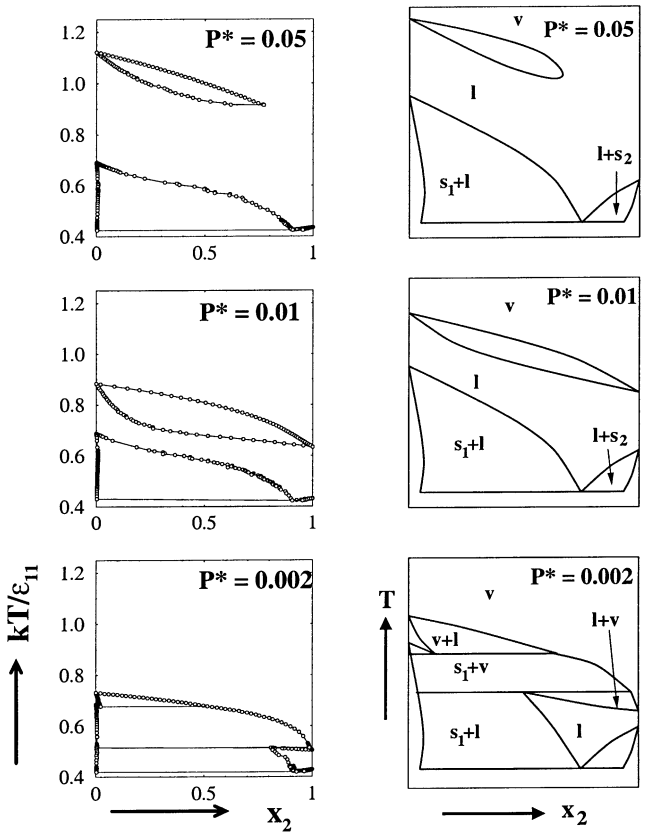

Fig. 4. Temperature–composition phase diagrams for a binary Lennard–Jones mixture with diameter ratio of 0.85 and a well-depth ratio of 1.6 at reduced pressures of $P^* = 0.002$, 0.01, and 0.05 [20]. The left-hand column shows the curves obtained by Gibbs–Duhem integration simulations; the right-hand column shows not-to-scale schematic phase diagrams corresponding to the simulation results. The labels identifying the phases present in each region are as in Fig. 3.

$P^* = 0.002, 0.01$, and 0.05 are shown along with not-to-scale schematics. At $P^* = 0.002$ the vapor–liquid and solid–liquid coexistence regions interfere. As pressure increases, the vapor–liquid coexistence region first shifts to higher temperatures ($P^* = 0.01$) and then begins to disappear ($P^* = 0.05$) as the pressure becomes higher than the critical pressure of pure component 2. It is convenient to summarize these results on a pressure–temperature projection that identifies the three-phase coexistence features of the mixture (solid–liquid–vapor and solid–solid–liquid) in addition to the pure component vapor–liquid, solid–liquid, and vapor–solid coexistence curves. The pressure–temperature projection for the binary Lennard–Jones mixture with ratios $\sigma_{11}/\sigma_{22} = 0.85$ and $\varepsilon_{11}/\varepsilon_{22} = 1.6$ is shown in Fig. 5. The pure component coexistence data (taken from the work of Kofke and coworkers [22,23]) are represented with solid lines. The eutectic (s_1s_2l) and solid(1)–liquid–vapor (s_1lg) temperatures determined from the simulations are shown by open circles, with dot-dashed lines connecting the points to guide the eye. The eutectic (s_1s_2l) locus is relatively independent of pressure. The solid(1)–liquid–vapor (s_1lg) locus originates from the triple point of pure component 1 and passes through a maximum pressure at $P^* = 0.005$. We anticipate that the s_1lg locus

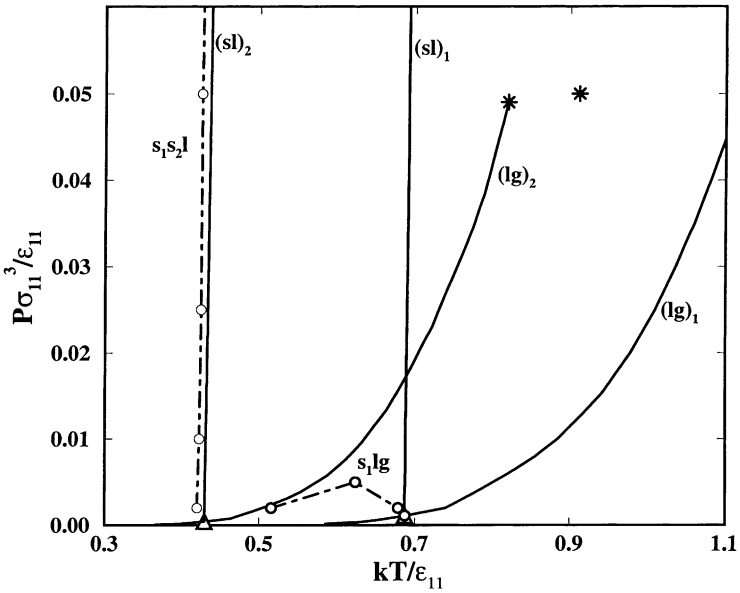

Fig. 5. Pressure–temperature projection for a binary Lennard–Jones mixture with diameter ratio of 0.85 and a well-depth ratio of 1.6. The open circles represent three-phase coexistence data from Gibbs–Duhem integration simulations. Dot-dashed lines are drawn through the simulation points as a guide to the eye. The remaining symbols are as follows: solid lines represent the pure component vapor pressure and melting curves, asterisks denote pure component and mixture vapor–liquid critical points, open triangles denote pure component triple points.

will terminate at the quadruple point (s_1s_2lg) of the mixture [44], which is below $P^* = 0.002$ (the lowest pressure considered). Our estimate of the binary mixture critical point at $P^* = 0.05$ is shown by an asterisk.

Pressure–temperature projections have been calculated for the remaining five mixtures mentioned above in order to observe how the features on these phase diagrams change with variations in diameter ratio σ_{11}/σ_{22} and well-depth ratio $\varepsilon_{11}/\varepsilon_{22}$. Highlights of these calculations (phase diagrams not shown) are the following. We find that as the diameter ratio decreases, the maximum in the locus of solid–liquid–vapor coexistence pressures decreases and the locus of solid(1)–solid(2)–liquid temperatures shifts from temperatures above the solid–liquid temperature of pure component 1 to temperatures below the solid–liquid coexistence temperature of pure component 1. We find that as well-depth ratio decreases, the coexistence curves for pure component 2 shift from temperatures and pressures below those of pure component 1 to temperatures and pressures above those of pure component 1 and that the maximum in the locus of solid–liquid–vapor coexistence pressures increases.

4. Summary

The Gibbs–Duhem integration technique was combined with semi-grand canonical Monte Carlo simulations to calculate temperature–composition and pressure–temperature phase diagrams for binary Lennard–Jones mixtures. This approach allows us to examine solid–liquid and solid–vapor phase

behavior of a mixture without resorting to a separate model for the solid state, thus, making it possible to classify phase diagrams based not only on fluid phase behavior, as was done by Van Konynenburg and Scott, but also on solid phase behavior.

Acknowledgements

This work was supported by the GAANN Computational Sciences Fellowship of the US Department of Education, and the Office of Energy Research, Basic Sciences, Chemical Science Division of the US Department of Energy under Contract no. DE-FG05-91ER14181. Acknowledgement is made to the donors of the Petroleum Research Fund administered by the American Chemical Society for partial support of this work.

References

[1] R.L. Scott, P.H. van Konynenburg, Discuss, Faraday Soc. 49 (1970) 87–97.
[2] P.H. Van Konynenburg, R.L. Scott, Phil. Trans. Roy. Soc. London A 298 (1980) 495–540.
[3] V.A. Mazur, L.Z. Boshkov, V.G. Murakhovsky, Phys. Lett. 104 (1984) 415–417.
[4] U.K. Deiters, I.L. Pegg, J. Chem. Phys. 90 (1989) 6632–6641.
[5] T. Kraska, U.K. Deiters, J. Chem. Phys. 96 (1992) 539–547.
[6] J.L. Wang, G.W. Wu, R.J. Sadus, Mol. Phys. 98 (2000) 715–723.
[7] M.E. van Leeuwen, C.J. Peters, J. de Swaan Arons, A.Z. Panagiotopoulos, Fluid Phase Equilib. 66 (1991) 57–75.
[8] M. Guo, Y. Li, Z. Li, J. Lu, Fluid Phase Equilib. 98 (1994) 129–139.
[9] J.N. Canongia Lopes, D.J. Tildesley, Mol. Phys. 92 (1997) 187–195.
[10] J.N. Canongia Lopes, Mol. Phys. 96 (1999) 1649–1658.
[11] R.J. Sadus, Fluid Phase Equilib. 157 (1999) 169–180.
[12] G.M. Schneider, in: M.L. McGlashan (Ed.), Chemical Thermodynamics, Vol. 2, Specialist Periodical Report, The Chemical Society, London, 1978, pp. 105–146.
[13] A. Smits, Proc. Koninklijke Akademie van Weterschappen 6 (1903) 171–181.
[14] V.M. Valyashko, Z. Phys. Chem. Leipzig 267 (3) (1986) 481–493.
[15] D.C. Garcia, K.D. Luks, Fluid Phase Equilib. 161 (1999) 91–106.
[16] J.A. Labadie, D.C. Garcia, K.D. Luks, Fluid Phase Equilib. 171 (2000) 11–26.
[17] M.J. Vlot, J.C. van Miltenburg, H.A.J. Oonk, J.P. van der Eerden, J. Chem. Phys. 107 (1997) 10102–10111.
[18] M.H. Lamm, C.K. Hall, AIChE J. 47 (2001) 1664–1675.
[19] M.H. Lamm, C.K. Hall, Fluid Phase Equilib. 182 (2001) 37–46.
[20] M.H. Lamm, C.K. Hall, J. Chem. Phys., submitted for publication.
[21] D.A. Kofke, Mol. Phys. 78 (1993) 1331–1336.
[22] D.A. Kofke, J. Chem. Phys. 98 (1993) 4149–4162.
[23] R. Agrawal, D.A. Kofke, Mol. Phys. 85 (1995) 43–59.
[24] M.R. Hitchcock, C.K. Hall, J. Chem. Phys. 110 (1999) 11433–11444.
[25] M. Mehta, D.A. Kofke, Chem. Eng. Sci. 49 (1994) 2633–2645.
[26] D.A. Kofke, E.D. Glandt, Mol. Phys. 64 (1988) 1105–1131.
[27] J.P. Hansen, L. Verlet, J. Chem. Phys. 184 (1969) 151–161.
[28] D.A. Kofke, Mol. Simul. 7 (1991) 285–302.
[29] J.L. Barrat, M. Baus, J.P. Hansen, Phys. Rev. Lett. 56 (1986) 1063–1065.
[30] J.L. Barrat, M. Baus, J.P. Hansen, J. Phys. C: Solid State Phys. 20 (1987) 1413–1430.
[31] W.G.T. Kranendonk, D. Frenkel, Mol. Phys. 72 (1991) 679–697.
[32] X. Cottin, P.A. Monson, J. Chem. Phys. 102 (1995) 3354–3360.
[33] H. Kruyt, Z. Physik. Ch. 79 (1912) 657–675.

[34] P.N. Walsh, N.O. Smith, J. Phys. Chem. 65 (1961) 718–721.
[35] C.G. de Kruif, A.C.G. van Genderen, J.C.W.B. Bink, H.A.J. Oonk, J. Chem. Thermodyn. 13 (1981) 457–463.
[36] S.A. Remyga, R.M. Myasnikova, A.I. Kitaigorodskii, Russ. J. Phys. Chem. 45 (1971) 328–330.
[37] F.B. Sprow, J.M. Prausnitz, AIChE J. 12 (1966) 780–784.
[38] S.C. Greer, L. Meyer, C.S. Barrett, J. Chem. Phys. 50 (1969) 4299–4304.
[39] P. van't Zelfde, M.H. Omar, H.G.M. le Pair-Schroten, Z. Dokoupil, Physica 38 (1968) 241–252.
[40] J.E. Ricci, The Phase Rule and Heterogeneous Equilibrium, Van Nostrand, London, 1951.
[41] J. Zernike, Chemical Phase Theory, Kluwer Academic Publishers, Deventer, 1955.
[42] M. Glaser, C.J. Peters, H.J. van der Kooi, R.N. Lichtenthaler, J. Chem. Thermodyn. 17 (1985) 803–815.
[43] H. Okamoto, J. Phase Equilib. 21 (2000) 109.
[44] A. Findlay, A.N. Campbell, N.O. Smith, The Phase Rule and Its Applications, Dover, New York, 1951.